

# Vibrational Properties in Highly Strained Hexagonal Boron Nitride Bubbles

Elena Blundo, Alessandro Surrente, Davide Spirito, Giorgio Pettinari, Tanju Yildirim, Carlos Alvarado Chavarin, Leonetta Baldassarre, Marco Felici, and Antonio Polimeni\*



Cite This: *Nano Lett.* 2022, 22, 1525–1533



Read Online

ACCESS |

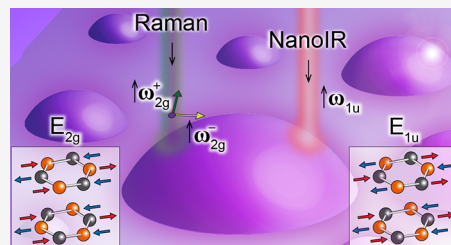
Metrics & More

Article Recommendations

SI Supporting Information

**ABSTRACT:** Hexagonal boron nitride (hBN) is widely used as a protective layer for few-atom-thick crystals and heterostructures (HSs), and it hosts quantum emitters working up to room temperature. In both instances, strain is expected to play an important role, either as an unavoidable presence in the HS fabrication or as a tool to tune the quantum emitter electronic properties. Addressing the role of strain and exploiting its tuning potentiality require the development of efficient methods to control it and of reliable tools to quantify it. Here we present a technique based on hydrogen irradiation to induce the formation of wrinkles and bubbles in hBN, resulting in remarkably high strains of ~2%. By combining infrared (IR) near-field scanning optical microscopy and micro-Raman measurements with numerical calculations, we characterize the response to strain for both IR-active and Raman-active modes, revealing the potential of the vibrational properties of hBN as highly sensitive strain probes.

**KEYWORDS:** strain, hBN, 2D materials, Raman, nano-IR, phonons



## I. INTRODUCTION

Hexagonal boron nitride (hBN), a wide-gap layered material,<sup>1</sup> features a marked chemical inertness<sup>2,3</sup> and mechanical robustness.<sup>4</sup> Thanks to these properties, hBN is an ideal substrate or capping material for two-dimensional crystals,<sup>5–10</sup> protecting them from oxidation<sup>11</sup> and bringing about a substantial improvement of the charge-carrier mobility and of the light emission characteristics.<sup>7,8,12</sup> Indeed, hBN capping is routinely employed to fabricate high-quality heterostructures (HSs), wherein intriguing carrier potential landscapes can be realized.<sup>13,14</sup> The fabrication process relies on mechanical stacking, often leading to the emergence of strain in the different layers and to important modifications of their electronic states.<sup>15</sup> hBN is also attracting increasing interest for its intrinsic properties, sustaining the propagation of hyperbolic phonon-polaritons (HPPs)<sup>16,17</sup> and hosting single-photon emitters operating at room temperature.<sup>18–22</sup> Its remarkable mechanical robustness (breaking strengths of ~70 GPa and Young's modulus of ~800 GPa<sup>4,23,24</sup>) was exploited for high-quality mechanical resonators<sup>25</sup> and to reversibly tune the emission wavelength of single-photon emitters via stretching.<sup>26</sup> Strained wrinkles were also found to be ideal candidates for launching HPPs.<sup>27</sup> It follows that in hBN, like in other two-dimensional materials, strain plays a relevant role.<sup>24</sup> Different methods were employed to induce strain in thin layers of hBN, for example, by deposition on substrates subject to stretching,<sup>26</sup> bending,<sup>28</sup> or thermal compression<sup>29</sup> or by nanoindentation.<sup>4</sup> Great attention was also attracted by the formation of hBN bubbles ensuing gas

trapping,<sup>30</sup> hydrogen-plasma exposure,<sup>31</sup> or pressure-induced bulging.<sup>23</sup> Such bubbles may be the ultimate platforms for probing the elastic/adhesive properties of two-dimensional materials, owing to the strong interplay between these properties and the bubble morphology.<sup>23,32–34</sup> Although hBN bubbles are expected to host sizable strains, as theoretically predicted and experimentally confirmed in similar graphene<sup>35</sup> and transition-metal dichalcogenide (TMD) structures,<sup>33,36–40</sup> where total strains of 1–5% were achieved, no clear evidence of strain has been provided so far. More generally, the effect of strain on the vibrational properties of thin hBN has surprisingly not received systematic attention, with only a few Raman studies published to date, focusing on the moderate strain regime (<0.4%).<sup>28,29,41</sup>

Here we report on a method to mechanically deform hBN based on the low-energy hydrogen (H) or deuterium (D) ion irradiation of multilayer flakes. Depending on the flake thickness, H/D-ion treatments lead to the formation of nano/micrometric bubbles or wrinkles. Unlike methods based on the deposition of ultrathin films,<sup>30</sup> the proposed technique permits the formation of wrinkles and bubbles with a high density and on flakes with virtually unrestricted size. In

Received: October 31, 2021

Revised: January 25, 2022

Published: February 2, 2022



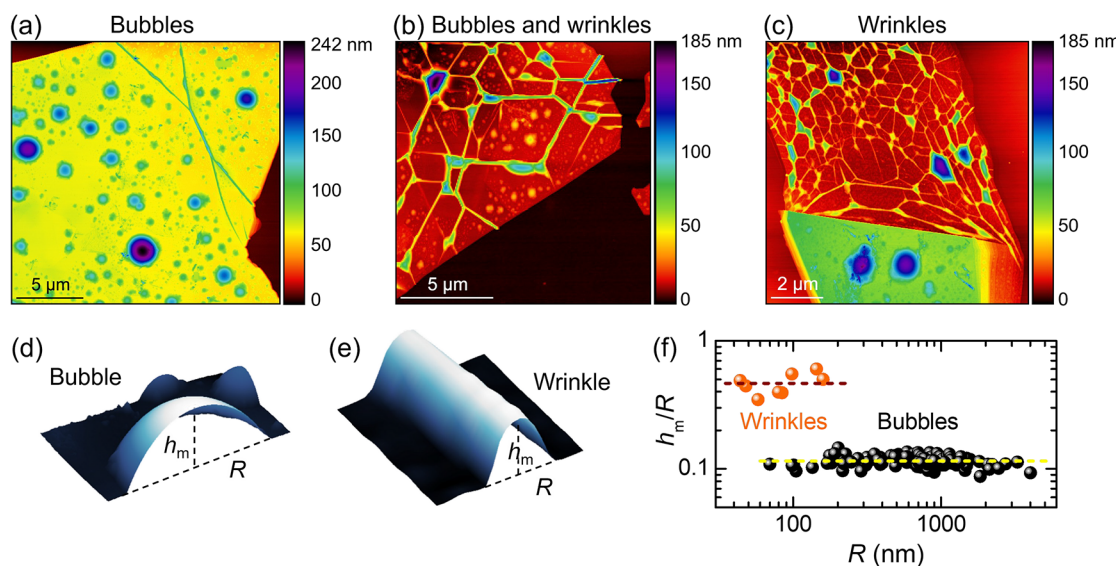


**Figure 1.** Formation of hydrogen-filled bubbles and of wrinkles in hBN. (a–c) AFM images of multilayer hBN flakes after H irradiation. The flakes have thicknesses of (a) 55, (b) 10, and (c) 5 nm (thin part corresponding to the top side of the figure), and the images show the presence of only bubbles, both bubbles and wrinkles, and only wrinkles, respectively. (d,e) 3D AFM images of half a bubble (panel d, where  $R = 2.06 \mu\text{m}$  and  $h_m = 225 \text{ nm}$ ) and part of a wrinkle (panel e, where  $R = 144 \text{ nm}$  and  $h_m = 88 \text{ nm}$ ). The definitions of maximum height ( $h_m$ ) and footprint radius ( $R$ ) are depicted. (f) Statistical analysis of the aspect ratios ( $h_m/R$ ) measured in wrinkles and bubbles. The dashed lines represent the average aspect ratios estimated for each set of data.

addition, we can control the thickness of the bubbles from a few layers to tens of layers by tuning the energy or changing the isotope of the ion beam. We employed an infrared (IR) scanning near-field optical microscope (SNOM) to perform nanoscale Fourier transform IR (nano-FTIR) measurements and an optical microscope to perform micro-Raman ( $\mu$ -Raman) measurements. Across the bubble surfaces, we observe record large shifts of both the IR-active and Raman-active modes in excess of  $50 \text{ cm}^{-1}$ . With the support of numerical modeling of the strain distribution, we extract the Grüneisen parameters of hBN and, by performing linearly polarized Raman spectroscopy, its shear deformation potential.

## II. RESULTS AND DISCUSSION

We exfoliated thick hBN flakes from commercial hBN crystals (HQ graphene). The flakes were deposited on Si/SiO<sub>2</sub> substrates and initially characterized by atomic force microscopy (AFM); see the Supporting Information, Methods. The samples were subjected to H (or D)-ion irradiation by a Kaufman ion gun<sup>37,42</sup> under high vacuum conditions at 150 °C, with the samples electrically grounded to avoid charging. For details, see the Supporting Information, Methods. To avoid the formation of defects, we employed low ion-beam energies of <35 eV. After the treatment, optical microscope images of the flakes may reveal a slightly nonhomogeneous coloration related to the presence of barely visible circular or elongated features; see Supporting Figure S1. AFM measurements demonstrate the presence of bubbles, wrinkles, or both on the flakes, as shown in Figure 1a–c and Supporting Figure S2. A statistical AFM study (see Supporting Figure S3) allows us to establish a correspondence between the different morphologies and the flake thickness  $t$ : For  $t \gtrsim 10 \text{ nm}$ , only bubbles form (Figure 1a); for  $t \approx 10 \text{ nm}$ , both bubbles and wrinkles can be observed (Figure 1b); and in thin flakes with  $t \lesssim 10 \text{ nm}$ , wrinkles and irregular structures predominate (Figure 1c). In the latter case, molecular hydrogen likely forms,

accumulates, and percolates at the flake/substrate interface, giving rise to irregular structures and wrinkles (Figure 1c); see also Supporting Figure S3. On the contrary, the formation of spherically shaped bubbles in thick flakes ( $t \gtrsim 10 \text{ nm}$ ) can be attributed to the formation and trapping of molecular hydrogen in the hBN interlayers, as observed in H-plasma-treated hBN,<sup>31</sup> and in TMDs.<sup>37</sup> We thus hypothesize that protons with kinetic energies of  $\sim 10$ –30 eV penetrate through hBN for  $\sim 10 \text{ nm}$  and that the formation of wrinkles or bubbles depends on where H<sub>2</sub> remains caged. To support this hypothesis, we intentionally induced the explosion of some bubbles via a high-power (some milliwatts), highly focused laser beam and measured the height difference between the crater of the exploded bubble and the flake surface outside the crater by AFM. In samples irradiated with H ions (beam energies <34 eV) (see Supporting Figure S4), we measured thicknesses ranging from 1.8 to 12 nm (corresponding to about 5 to 36 monolayers). To form thinner bubbles, instead, we irradiated some samples with deuterium ions (beam energies <25 eV), which are known to penetrate less through hBN with respect to protons,<sup>43</sup> and we measured bubble thicknesses as thin as  $\sim 0.5 \text{ nm}$  (i.e., a couple of layers); see Supporting Figure S4. This demonstrates the remarkable flexibility of our method, which, unlike H-plasma-based methods,<sup>31</sup> enables us to obtain bubbles thinner than 10 monolayers. The long durability of the bubbles and Raman studies of the irradiated flakes (see Supporting Figure S5) suggest that the low-energy beams employed here do not induce a sizable amount of defects in the crystal, unlike higher energy heavier atom beams.<sup>44–50</sup>

We performed AFM measurements to study the morphological properties of bubbles and wrinkles and measured their aspect ratio  $h_m/R$ , where  $h_m$  is the maximum height of the object and  $R$  is its half width. (See Figure 1d,e). The results are summarized in Figure 1f. The wrinkles feature a narrow width distribution and aspect ratios in the 0.3 to 0.6 range. The bubbles show a much wider size distribution and a size-

independent aspect ratio, as expected based on previous theoretical<sup>30,32,51</sup> and experimental<sup>30–32,37,38,52</sup> studies. For our bubbles, we find  $h_m/R = 0.115 \pm 0.011$ , in agreement with that reported for hydrocarbon-filled monolayer bubbles<sup>30</sup> and multilayer bubbles created by H-plasma treatments.<sup>31</sup> The constant aspect ratio, independent of size and thickness, testifies that the mechanics of the bubbles is dominated by stretching, whereas the bending contribution is negligible,<sup>32,53</sup> at variance with other kinds of bent, yet not pressurized, systems.<sup>54</sup> Importantly, the strain scales as  $(h_m/R)^2$ ,<sup>32</sup> therefore, a similar strain distribution is expected independent of the bubble formation method and thickness. Next, we address such distribution on hBN bubbles.

One of the most common means for evaluating the amount of strain in two-dimensional materials is provided by a quantitative analysis of the frequency of the lattice vibration normal modes.<sup>24</sup> Typically, lattice stretching (i.e., tensile strain) induces a softening of the phonon modes. Furthermore, under anisotropic strains, the double-degenerate in-plane modes split as a result of the lowered crystal symmetry. The shift rate and splitting rate of the vibrational modes can thus be conveniently used to assess the strain magnitude and its anisotropy degree in atomically thin membranes.<sup>24</sup> This is especially important when the actual strain differs from the expected strain, like in many bending or stretching devices,<sup>24</sup> or cannot be estimated theoretically. In this work, we focus on two specific in-plane transverse modes, which are IR-active ( $E_{1u}$ ) and Raman-active ( $E_{2g}$ ). Their lattice displacements are sketched in Figure 2.

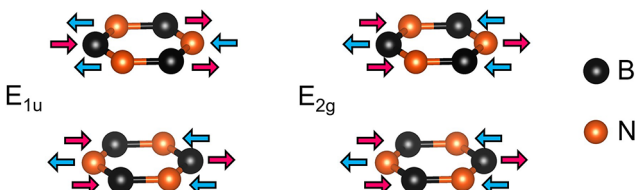


**Figure 2.** Sketch of the atom displacements corresponding to the IR-active  $E_{1u}$  mode and to the Raman-active  $E_{2g}$  mode. Differently colored arrows indicate opposite atom motions.

Figure 3a displays the AFM image of a circular hBN bubble with diameter  $D = 2R = 4.54 \mu\text{m}$  and height  $h_m = 267 \text{ nm}$  ( $h_m/R = 0.117$ ) obtained by D irradiation. The AFM profile recorded along the cyan dashed line is shown in Figure 3b (circles). The yellow line is the profile evaluated by finite element method (FEM) numerical calculations; see the Supporting Information, Methods. The latter also provides the strain distribution,<sup>32,37</sup> as shown on the left side of Figure 3c, where  $\varepsilon_r$  and  $\varepsilon_\theta$  are the radial and circumferential in-plane strain components in polar coordinates, respectively.<sup>32,53</sup> The calculated spatial distribution of the total strain  $\varepsilon_{\text{tot}} = \varepsilon_r + \varepsilon_\theta$  is displayed as a false-color image on the right side of panel c. Strain features an anisotropic character, changing from tensile uniaxial at its edge ( $r/R = 1$ ,  $\varepsilon_r \neq 0$  and  $\varepsilon_\theta = 0$ ) to tensile equibiaxial at the summit of the bubble ( $r/R = 0$ ,  $\varepsilon_r = \varepsilon_\theta$ ). On these premises, we expect the in-plane transverse phonon frequency  $\omega_t$  to undergo a decrease with respect to unstrained hBN due to stretching, as well as a splitting in  $\omega_t^+$  and  $\omega_t^-$ , the extent of which depends on the position on the bubble. Thus we introduce the average frequency

$$\omega_t^{\text{av}} = \frac{\omega_t^+ + \omega_t^-}{2} \quad (1)$$

and mode splitting

$$\sigma_t = \omega_t^+ - \omega_t^- \quad (2)$$

The frequency variation upon strain can be quantified by the shift rate

$$\Delta = -\frac{\partial \omega_t^{\text{av}}}{\partial \varepsilon_{\text{tot}}} \quad (3)$$

and splitting rate

$$\Sigma = \frac{\partial \sigma_t}{\partial \varepsilon_{\text{diff}}} \quad (4)$$

where  $\varepsilon_{\text{tot}}(r) = \varepsilon_r(r) + \varepsilon_\theta(r)$  and  $\varepsilon_{\text{diff}}(r) = \varepsilon_r(r) - \varepsilon_\theta(r)$ .

Equivalently, one can introduce dimensionless quantities, such as the Grüneisen parameter

$$\gamma = \frac{\Delta}{\omega_t^0} \quad (5)$$

and the shear deformation potential

$$\beta = \frac{\Sigma}{\omega_t^0} \quad (6)$$

where  $\omega_t^0$  is the mode frequency in the absence of strain.

The  $E_{1u}$  mode (see lattice displacements in Figure 2) was studied by nano-FTIR SNOM measurements;<sup>55,56</sup> see the Supporting Information, Methods. This technique has been widely employed in two-dimensional systems, for example, to probe phonon-polaritons in hBN,<sup>27,57,58</sup> phonons in hBN superlattices,<sup>59</sup> electron–phonon interactions in graphene,<sup>60</sup> and intersubband transitions in two-dimensional quantum wells,<sup>61</sup> but the  $E_{1u}$  hBN mode sensitivity to strain has not been investigated, to our knowledge. Figure 3d shows the normalized near-field amplitude  $S(\omega, r)$ , as obtained with a spectral line scan along the gray short dashed line in Figure 3a. The near-field signal originates from the tip–sample interaction and provides a lateral resolution of  $\sim 20 \text{ nm}$ ; see the Supporting Information, Methods. The corresponding spectra are shown in Figure 3e. The phonon peak frequency from the bulk region outside the bubble is  $\omega_{1u} = 1367 \text{ cm}^{-1}$ , in agreement with previous reports.<sup>62</sup> An abrupt decrease in  $\omega_{1u}$  is noticed when the tip approaches the bubble’s edge, where a 0.9% tensile strain is already present. (See Figure 3c.) On moving further toward the bubble center,  $\omega_{1u}$  seamlessly decreases, in agreement with the expected tensile strain increase. To quantify the mode shift variation versus the total strain  $\varepsilon_{\text{tot}}(r)$ , we established a one-to-one correspondence between the AFM-derived bubble profile ( $h$  vs  $r$ ) and the calculated strain components shown in Figure 3c. In turn, this allowed us to establish a correspondence between each measured  $\omega_{1u}$  and  $\varepsilon_{\text{tot}}(r)$ , given that the  $h(r)$  values were measured by the SNOM tip at the very same points where  $\omega_{1u}$  was probed. To reduce the background signal, we collected the near-field data at several harmonics. In Figure 3f, we show the spatial dependence of the second and third harmonics of the signal associated with the  $E_{1u}$  phonon. (See the Supporting Information, Methods and Supporting Note 1.) We reproduce quite successfully the dependence of  $\omega_{1u}$  on  $r$  using as fitting parameters the mode frequency at zero strain  $\omega_{1u}^0 = (1369.7 \pm$

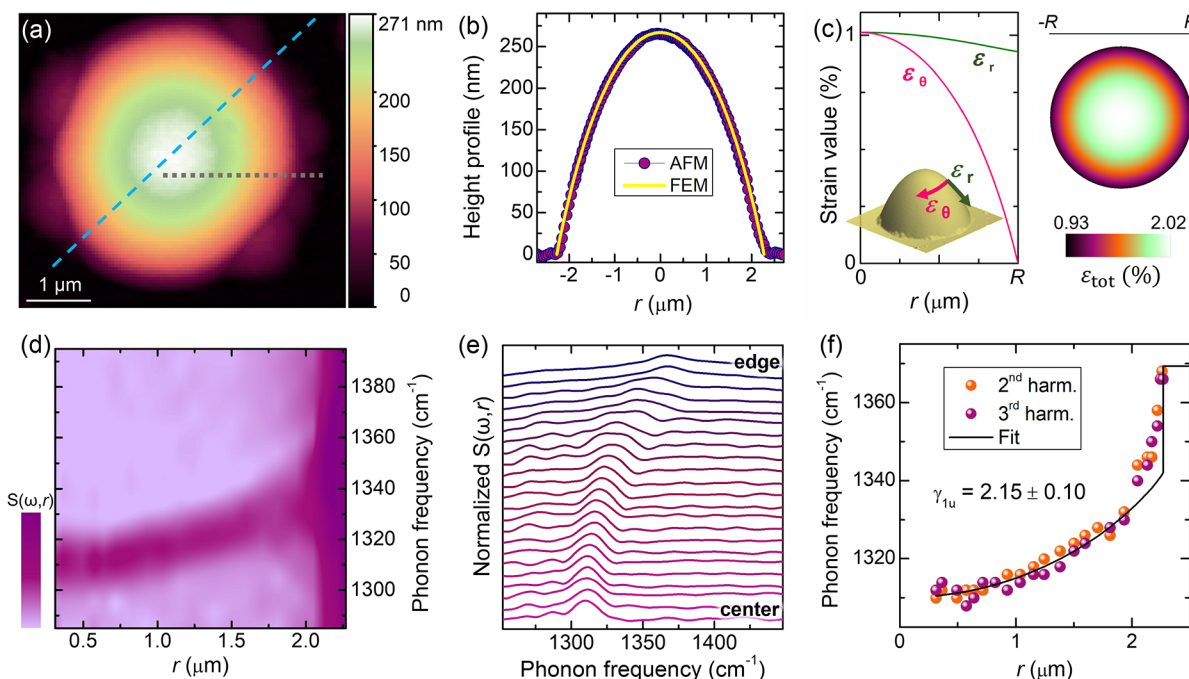


**Figure 3.** IR-active mode versus strain. (a) 2D AFM image of a hBN bubble exhibiting a circular symmetric shape but on its edge, where smaller satellite bubbles nucleated. The bubble has  $R = 2.27 \mu\text{m}$  and  $h_m = 267 \text{ nm}$  ( $h_m/R = 0.117$ ) and was created in a deuterated sample (beam energy equal to 6 eV) to minimize the bubble thickness. (b) Comparison between the AFM profile acquired along a diameter of the bubble (highlighted in panel a by a cyan dashed line) and the profile obtained by FEM calculations. (c) Left: Radial dependence, obtained by FEM calculations, of the in-plane circumferential ( $\varepsilon_\theta$ ) and radial ( $\varepsilon_r$ ) strain components, a sketch of which is depicted as the inset. Right: Spatial distribution of the total in-plane strain  $\varepsilon_{\text{tot}} = \varepsilon_r + \varepsilon_\theta$ . (d,e) Color map of the near-field amplitude  $S(\omega, r)$  (d) and corresponding spectra (e), where the IR-active mode ( $E_{1u}$ ) is visible. The measurements were taken along the gray short dashed line shown in panel a. The second harmonic is considered here. (f) IR phonon frequency dependence on the radial distance  $r$ , as deduced from the spectra shown in panel e and the AFM profile. The third-harmonic data are also included here. The black solid line is a fit to the data assuming a linear dependence of the phonon frequency on  $\varepsilon_{\text{tot}}$  provided by eqs 3 and 5.

**Table 1. Effect of Strain on the Vibrational Modes<sup>a</sup>**

mode	$\omega_t^0$ (cm <sup>-1</sup> )	$\Delta$ (cm <sup>-1</sup> /%)	$\gamma_t$	$\Sigma_t$ (cm <sup>-1</sup> /%)	$\beta_t$	$\beta_t/\gamma_t$
$E_{1u}$ (IR)	$1369.9 \pm 2.3$	$29.4 \pm 1.8$	$2.15 \pm 0.12$			
	$1369.7 \pm 2.4$	$29.5 \pm 1.4$	$2.15 \pm 0.10$			
	$1369.0 \pm 5.2$	$36.2 \pm 3.6$	$2.64 \pm 0.27$			
$E_{2g}$ (Raman)	$1370^b$	$24.6 \pm 0.60$	$1.79 \pm 0.04$	$11.2 \pm 1.9$	$0.82 \pm 0.14$	$0.46 \pm 0.08$
	$1370^b$	$25.1 \pm 4.5$	$1.83 \pm 0.33$			
	$1370^b$	$28.5 \pm 8.4$	$2.08 \pm 0.61$	$15.6 \pm 3.8$	$1.14 \pm 0.28$	$0.56 \pm 0.14$
	$1370^b$	$33.2 \pm 5.2$	$2.43 \pm 0.40$			

<sup>a</sup>Parameters obtained for the  $E_{1u}$  and  $E_{2g}$  from the nano-FTIR and Raman measurements, respectively. The frequency at zero strain ( $\omega_t^0$ ), shift rate ( $\Delta$ ), Grüneisen parameter ( $\gamma_t$ ), splitting rate ( $\Sigma_t$ ), shear deformation potential ( $\beta_t$ ), and ratio  $\gamma_t/\beta_t$  were estimated for several bubbles. <sup>b</sup>This value was kept fixed because it was otherwise affected by too large uncertainties.

2.4) cm<sup>-1</sup> and the shift rate  $\Delta_{1u} = (29.5 \pm 1.4)$  cm<sup>-1</sup>/%, resulting in a Grüneisen parameter (see eq 5)  $\gamma_{1u} = 2.15 \pm 0.10$ . Analogous measurements were performed on other bubbles; see Supporting Note 1 and Table 1.

It should be noticed that the zero-strain limit  $\omega_{1u}^0$  (~1370 cm<sup>-1</sup>) of the bubble  $E_{1u}$  mode is larger than that of bulk hBN (~1367 cm<sup>-1</sup>). This is consistent with the frequency increase reported for the Raman-active  $E_{2g}$  mode in the few-layer limit.<sup>29,63,64</sup>

Let us now discuss our studies of the  $E_{2g}$  mode. (See the lattice displacements in Figure 2.) We performed  $\mu$ -Raman measurements of the hBN bubble ( $R = 1.61 \mu\text{m}$ ,  $h_m = 179 \text{ nm}$ ,  $h_m/R = 0.111$ , created by D irradiation), whose AFM image is shown as the inset of Figure 4c. Figure 4a is the spectrally and spatially resolved intensity map of the light scattered by the bubble in the spectral region of the  $E_{2g}$  mode. The map was

recorded along a diameter (see the inset of panel c), and the corresponding spectra are shown in Figure 4b. The spot size and spectral resolution are ~0.5 μm and 0.7 cm<sup>-1</sup>, respectively; see the Supporting Information, Methods. The intense peak at 1366.2 cm<sup>-1</sup> comes from the bulk hBN flake from which the bubble swelled. The  $E_{2g}$  signal from the bubble is much less intense due to the reduced thickness and exhibits a spatially dependent and lower frequency due to strain. We notice that unlike the IR signal, the Raman signal becomes negligibly small as the laser approaches the edge of the bubble due to optical interference effects.<sup>37,39</sup> The correspondence between the measured  $\omega_{2g}$  values and  $\varepsilon_{\text{tot}}(r) = \varepsilon_r(r) + \varepsilon_\theta(r)$  is established by evaluating the strain via FEM calculations based on the AFM profile; see Supporting Figure S6. The spatial dependence of  $\omega_{2g}$  is shown in Figure 4c, and it is best reproduced with a shift rate  $\Delta_{2g} = (28.5 \pm 8.4)$  cm<sup>-1</sup>/% and a Grüneisen

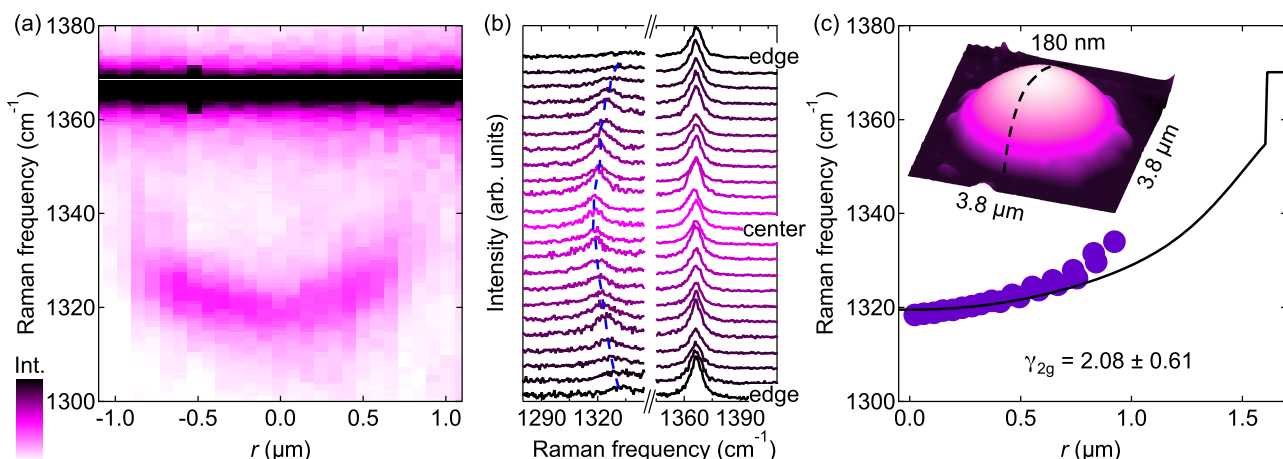


**Figure 4.** Raman-active mode versus strain. (a) False-color image of the intensity of the  $E_{2g}$  Raman mode as a function of the position along a diameter of a bubble. The bubble has  $R = 1.61 \mu\text{m}$  and  $h_m = 179 \text{ nm}$  ( $h_m/R = 0.111$ ) and was created in a deuterated sample (beam energy equal to 25 eV). (b) Raman spectra corresponding to the map of panel a. (c)  $E_{2g}$  Raman-mode frequencies as a function of the distance from the center of the bubble. The solid line is a linear fit to the frequency versus  $r$  behavior, with  $\gamma_{2g}$  being the fitting parameter. Inset: AFM image of the investigated structure. The dashed line indicates the diameter along which the spectra were measured.

parameter (see eq 5)  $\gamma_{2g} = 2.08 \pm 0.61$ . The extrapolation frequency at zero strain was set at  $1370 \text{ cm}^{-1}$ , which is greater than the corresponding bulk mode ( $1366.2 \text{ cm}^{-1}$ ), like in the case of the  $E_{1u}$  IR-active mode and consistent with published results.<sup>29,63,64</sup> Similar measurements performed on different bubbles are shown in Supporting Note 2, and the estimated parameters are displayed in Table 1. We also performed a statistical analysis of the shift at the bubble summit including many other bubbles, giving average Grüneisen parameters  $\gamma_{2g} = 2.04 \pm 0.48$  ( $\Delta_{2g} = (27.9 \pm 6.6) \text{ cm}^{-1}/\%$ ); see Supporting Note 3. Our statistical analysis also shows how  $E_{1u}$  and  $E_{2g}$  are characterized by similar Grüneisen parameters.

Previous  $\mu$ -Raman studies on hBN bubbles created by H-plasma treatments<sup>31</sup> reported only a modest shift of  $\sim 3 \text{ cm}^{-1}$  between the bubble center and the bulk hBN. Similar small shifts ( $\sim 3 \text{ cm}^{-1}$ ) were observed in hBN monolayers subject to thermal compression (biaxial strain of  $-0.17\%$ ),<sup>29</sup> resulting in  $\gamma_{2g} = 0.62$ . Finally, uniaxial strains of up to 0.4% were applied to thin hBN flakes (two to four layers) using a bending apparatus, achieving frequency softenings of  $< 6 \text{ cm}^{-1}$ . Grüneisen parameters  $\gamma_{2g}$  between 1.77 and 2.07 were estimated in this case<sup>28</sup> and were, on average, slightly lower than our estimates. (See Table 1.) By comparison with the current literature, our approach permits us to achieve a much larger total strain, on average, equal to  $\sim 1.9\%$ , with unprecedented shifts in excess of  $50 \text{ cm}^{-1}$ .

In addition to the  $E_{2g}$  mode shift, a splitting is expected in the bubbles due to the imbalance between  $\varepsilon_\theta$  and  $\varepsilon_r$ ; see Supporting Figure S6. Figure 5a displays an intensity map formed by polarization-dependent  $\mu$ -Raman spectra recorded on a given point of the same bubble of Figure 4. The point is 790 nm away from the center (i.e.,  $r/R = 0.49$ ) and is marked by a black dot superimposed on the strain anisotropy degree plot in Figure 5c, with the anisotropy being defined as  $\alpha = (\varepsilon_r - \varepsilon_\theta)/(\varepsilon_r + \varepsilon_\theta)$ . Therein, the arrows indicate the strain direction. The radial distance  $r$  was determined by the relationship between  $\omega_{2g}$  and  $r$  given in Figure 4c. Each spectrum of Figure 5a was recorded by keeping the polarization direction of the laser fixed at an arbitrary, unknown angle  $\phi_0$  with respect to a reference crystal direction (e.g., the armchair/zigzag direction). Likewise, strain is

oriented along the bubble radius, and its direction is thus also fixed at an unknown angle  $\theta$  with respect to the same lattice reference. The angle  $\phi$  between the polarization of the Raman-scattered and Raman-exciting photons was then varied from 0 to  $360^\circ$ . Whereas the  $E_{2g}$  bulk mode at  $1366.2 \text{ cm}^{-1}$  remains constant in intensity and frequency, the strain-softened  $E_{2g}$  mode of the bubble in the  $1320$ – $1340 \text{ cm}^{-1}$  range exhibits a marked angular dependence of its center-of-mass frequency, pointing to a mode splitting. This is exemplified in Figure 5b, showing two  $\mu$ -Raman spectra recorded with opposite polarizations ( $\phi = 0$  and  $90^\circ$ ). Indeed, it can be demonstrated that the intensities  $I_{2g}^\pm$  of the  $E_{2g}^\pm$  modes split by uniaxial strain are given by<sup>24</sup>

$$\begin{aligned} I_{2g}^+ &= c^2 \cos^2(\phi + 2\phi_0 + \theta) \\ I_{2g}^- &= c^2 \sin^2(\phi + 2\phi_0 + \theta) \\ I_{2g} &= I_{2g}^+ + I_{2g}^- = c^2 \end{aligned} \quad (7)$$

where  $c$  is a constant. By performing a line-shape fitting of the Raman spectra (see Supporting Note 4), we extracted  $I_{2g}^\pm$  as a function of  $\phi$ , where  $E_{2g}^+$  and  $E_{2g}^-$  refer to the high- and low-frequency components, respectively. Figure 5d shows the resulting polar plot obtained from the data of panel a. The reference angle ( $2\phi_0 + \theta$ ) is set to zero for simplicity reasons. The two components are clearly in counter phase, as expected. Figure 5e shows a similar set of measurements acquired on a point of the bubble positioned symmetrically at  $90^\circ$  with respect to the previous one (at  $r = 680 \text{ nm}$ ); see the gray dot in panel c. In this case, the strain direction is given by  $\theta' = \theta + 90^\circ$ , and as a consequence of eq 7, the  $E_{2g}^\pm$  components follow an angular dependence that is  $\pi/2$  out-of-phase with respect to that of the previous point (Figure 5d). These results are fully consistent with the strain field calculated numerically, whereby the  $\varepsilon_r$  component dictates the strain direction. Finally, the  $\mu$ -Raman spectra recorded at the bubble center (white dot in panel c), where the strain is equi-biaxial, show no mode splitting; see Figure 5f. Other polarization maps were acquired in different points of the bubble. For each point, the average frequency  $\omega_{2g}^{\text{av}}$  corresponds to a given  $r$  value. (See Figure 4c.) In turn, via numerical simulations (see Supporting Figure S6),

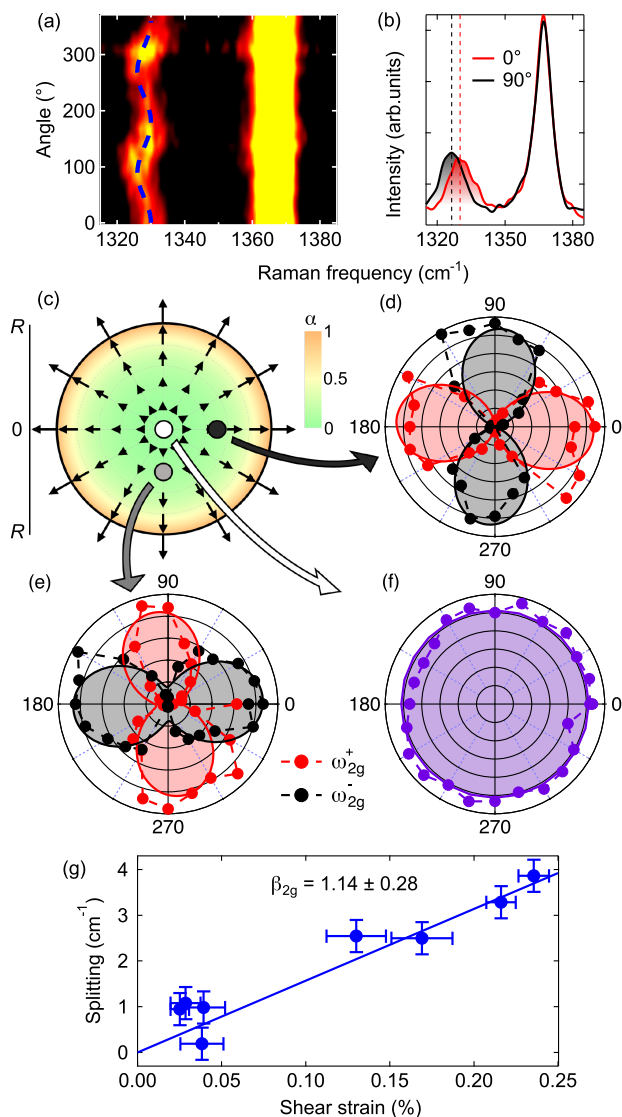


**Figure 5.** (a) False-color map of the intensity of the  $E_{2g}$  Raman mode as a function of the angle of the polarization analyzer. The dashed line is a sinusoidal guide to the eye. (b)  $\mu$ -Raman spectra measured with polarizations parallel and perpendicular to the uniaxial strain direction. (c) Radial dependence of the strain anisotropy  $\alpha = (\epsilon_r - \epsilon_\theta)/(\epsilon_r + \epsilon_\theta)$ , based on FEM calculations. The arrows point to the direction of the strain field. Their length is calculated as  $\log_{10}(100\alpha)$ . The dots depict the position of the excitation spots of the polarization-resolved Raman measurements. (d–f) Intensity of the low-frequency ( $\omega_{1u}^-$ ) and high-frequency ( $\omega_{1u}^+$ ) Raman modes as a function of the analyzer angle for excitation performed (d) on the right (black dot), (e) at the bottom (gray dot), and (f) at the center of a bubble (white dot). (g) Mode splitting as a function of the shear strain. The solid line is a linear fit.

we obtain  $\epsilon_{\text{shear}}(r) = \epsilon_{\text{diff}}(r) = \epsilon_r(r) - \epsilon_\theta(r)$ . Figure 5g shows the dependence of the mode splitting  $\sigma_{2g}$  versus  $\epsilon_{\text{shear}}(r)$ . Considering eq 6, we estimate a splitting rate  $\Sigma_{2g} = 15.6 \pm 3.8 \text{ cm}^{-1}/\%$  and a shear deformation potential  $\beta_{2g} = 1.14 \pm 0.28$ . Thus for this bubble, we get  $\beta_{2g}/\gamma_{2g} = 0.56 \pm 0.14$ . We performed similar measurements on another bubble with a lower Grüneisen parameter (see Supporting Note 4) and found  $\beta_{2g} = 0.82 \pm 0.14$  and  $\beta_{2g}/\gamma_{2g} = 0.46 \pm 0.08$  (see Table 1), showing how the ratio  $\beta_{2g}/\gamma_{2g}$  is less affected by fluctuations than  $\beta_{2g}$  and  $\gamma_{2g}$ . We are aware of only one previous report of

the hBN shear potential in the few-layer limit, where the ratio  $\beta_{2g}/\gamma_{2g}$  was found to vary between 0.45 and 0.52.<sup>28</sup>

### III. CONCLUSIONS

We irradiated bulk hBN flakes with low-energy hydrogen or deuterium ions. The ions penetrate through the crystal for a few nanometers, and molecular hydrogen or deuterium forms, inducing the blistering of a few atomic planes and hence the formation of micro/nano-metric wrinkles or bubbles. Wrinkles or bubbles predominate for flake thicknesses of  $t \lesssim 10 \text{ nm}$  or  $\gtrsim 10 \text{ nm}$ , respectively. The bubbles were investigated in detail because they exhibit tensile strains with a remarkably high  $\sim 2\%$  maximum value, exceeding that typically achieved for hBN in bending/stretching devices.<sup>28,29,41</sup> The effects of strain on the IR-active ( $E_{1u}$ ) and Raman-active ( $E_{2g}$ ) in-plane modes were studied over the bubble surface by spatially resolved nano-FTIR and polarization-dependent  $\mu$ -Raman, respectively. The large amount of strain and its anisotropic character toward the edge of the bubbles permitted to derive shift and splitting rates on the order of 30 and  $15 \text{ cm}^{-1}/\%$ , respectively. These values are comparable to those reported in graphene and are about one order of magnitude larger than those found in TMDs, InSe, and black phosphorus.<sup>24</sup> These findings show that the vibrational properties of hBN are extremely sensitive probes of mechanical deformations, and thus they can be exploited to assess the stress status of two-dimensional HSs and hBN-based quantum emitters.

### ■ ASSOCIATED CONTENT

#### Supporting Information

The Supporting Information is available free of charge at <https://pubs.acs.org/doi/10.1021/acs.nanolett.1c04197>.

Methods section and notes on IR-SNOM and Raman mapping or statistical measurements and of polarization-resolved Raman measurements in hBN bubbles, additional optical and AFM images of hBN bubbles and wrinkles, and additional FEM calculations (PDF)

### ■ AUTHOR INFORMATION

#### Corresponding Author

Antonio Polimeni — Physics Department, Sapienza University of Rome, 00185 Rome, Italy; [orcid.org/0000-0002-2017-4265](https://orcid.org/0000-0002-2017-4265); Email: [antonio.polimeni@uniroma1.it](mailto:antonio.polimeni@uniroma1.it)

#### Authors

Elena Blundo — Physics Department, Sapienza University of Rome, 00185 Rome, Italy; [orcid.org/0000-0003-0423-4798](https://orcid.org/0000-0003-0423-4798)

Alessandro Surrente — Physics Department, Sapienza University of Rome, 00185 Rome, Italy; Department of Experimental Physics, Faculty of Fundamental Problems of Technology, Wroclaw University of Science and Technology, Wroclaw 50-370, Poland; [orcid.org/0000-0003-4078-4965](https://orcid.org/0000-0003-4078-4965)

Davide Spirito — IHP-Leibniz Institut fur Innovative Mikroelektronik, 15236 Frankfurt (Oder), Germany; [orcid.org/0000-0002-6074-957X](https://orcid.org/0000-0002-6074-957X)

Giorgio Pettinari — Institute for Photonics and Nanotechnologies (CNR-IFN), National Research Council, 00156 Rome, Italy

**Tanju Yildirim** – *Center for Functional Sensor & Actuator (CFSN), National Institute for Materials Science (NIMS), Tsukuba, Ibaraki 305-0044, Japan*

**Carlos Alvarado Chavarin** – *IHP-Leibniz Institut für Innovative Mikroelektronik, 15236 Frankfurt (Oder), Germany*

**Leonetta Baldassarre** – *Physics Department, Sapienza University of Rome, 00185 Rome, Italy; IHP-Leibniz Institut für Innovative Mikroelektronik, 15236 Frankfurt (Oder), Germany*

**Marco Felici** – *Physics Department, Sapienza University of Rome, 00185 Rome, Italy*

Complete contact information is available at:  
<https://pubs.acs.org/10.1021/acs.nanolett.1c04197>

## Notes

The authors declare no competing financial interest.

## ACKNOWLEDGMENTS

We thank Emmanuele Cappelluti and Habib Rostami for useful discussions and Yuerui Lu for previous work in the field. A.P. and M.F. acknowledge support by Sapienza Università di Roma under grants “Ricerche Ateneo” 2018 and 2019 and “Progetti H2020-Collaborativi”. E.B., A.P., and M.F. acknowledge funding from the Regione Lazio programme “Progetti di Gruppi di ricerca” legge Regionale n. 13/2008 (SINFONIA project, prot. n. 85-2017-15200) via LazioInnova spa. A.S. gratefully acknowledges funding from the European Union’s Horizon 2020 research and innovation programme under the Marie Skłodowska-Curie grant agreement no. 844837. L.B. acknowledges support from the PRIN2017 grant number 2017Z8TSSB and from the IHP Microelectronics “Wolfgang Mehr” Fellowship Award.

## REFERENCES

- (1) Watanabe, K.; Taniguchi, T.; Kanda, H. Direct-bandgap properties and evidence for ultraviolet lasing of hexagonal boron nitride single crystal. *Nat. Mater.* **2004**, *3*, 404–409.
- (2) Liu, Z.; Gong, Y.; Zhou, W.; Ma, L.; Yu, J.; Idrobo, J. C.; Jung, J.; MacDonald, A. H.; Vajtai, R.; Lou, J.; Ajayan, P. M. Ultrathin high-temperature oxidation-resistant coatings of hexagonal boron nitride. *Nat. Commun.* **2013**, *4*, 2541.
- (3) Li, L. H.; Cervenka, J.; Watanabe, K.; Taniguchi, T.; Chen, Y. Strong oxidation resistance of atomically thin boron nitride nanosheets. *ACS Nano* **2014**, *8*, 1457–1462.
- (4) Falin, A.; Cai, Q.; Santos, E. J.; Scullion, D.; Qian, D.; Zhang, R.; Yang, Z.; Huang, S.; Watanabe, K.; Taniguchi, T.; Barnett, M. R.; Chen, Y.; Ruoff, R. S.; Li, L. H. Mechanical properties of atomically thin boron nitride and the role of interlayer interactions. *Nat. Commun.* **2017**, *8*, 15815.
- (5) Raja, A.; Waldecker, L.; Zipfel, J.; Cho, Y.; Brem, S.; Ziegler, J. D.; Kulig, M.; Taniguchi, T.; Watanabe, K.; Malic, E.; et al. Dielectric disorder in two-dimensional materials. *Nat. Nanotechnol.* **2019**, *14*, 832–837.
- (6) Dean, C. R.; Young, A. F.; Meric, I.; Lee, C.; Wang, L.; Sorgenfrei, S.; Watanabe, K.; Taniguchi, T.; Kim, P.; Shepard, K. L.; Hone, J. Boron nitride substrates for high-quality graphene electronics. *Nat. Nanotechnol.* **2010**, *5*, 722–726.
- (7) Cadiz, F.; Courtade, E.; Robert, C.; Wang, G.; Shen, Y.; Cai, H.; Taniguchi, T.; Watanabe, K.; Carrere, H.; Lagarde, D.; Manca, M.; Amand, T.; Renucci, P.; Tongay, S.; Marie, X.; Urbaszek, B. Excitonic linewidth approaching the homogeneous limit in MoS<sub>2</sub>-based van der Waals heterostructures. *Phys. Rev. X* **2017**, *7*, No. 021026.
- (8) Ajayi, O. A.; Ardelean, J. V.; Shepard, G. D.; Wang, J.; Antony, A.; Taniguchi, T.; Watanabe, K.; Heinz, T. F.; Strauf, S.; Zhu, X.-Y.; Hone, J. C. Approaching the intrinsic photoluminescence linewidth in transition metal dichalcogenide monolayers. *2D Mater.* **2017**, *4*, No. 031011.
- (9) Chen, X.; Wu, Y.; Wu, Z.; Han, Y.; Xu, S.; Wang, L.; Ye, W.; Han, T.; He, Y.; Cai, Y.; Wang, N. High-quality sandwiched black phosphorus heterostructure and its quantum oscillations. *Nat. Commun.* **2015**, *6*, 7315.
- (10) Mayorov, A. S.; Gorbachev, R. V.; Morozov, S. V.; Britnell, L.; Jalil, R.; Ponomarenko, L. A.; Blake, P.; Novoselov, K. S.; Watanabe, K.; Taniguchi, T.; Geim, A. K. Micrometer-scale ballistic transport in encapsulated graphene at room temperature. *Nano Lett.* **2011**, *11*, 2396–2399.
- (11) Arora, H.; Jung, Y.; Venanzi, T.; Watanabe, K.; Taniguchi, T.; Hübner, R.; Schneider, H.; Helm, M.; Hone, J. C.; Erbe, A. Effective Hexagonal Boron Nitride Passivation of Few-Layered InSe and GaSe to Enhance Their Electronic and Optical Properties. *ACS Appl. Mater. Interfaces* **2019**, *11*, 43480.
- (12) Wierzbowski, J.; Klein, J.; Sigger, F.; Straubinger, C.; Kremser, M.; Taniguchi, T.; Watanabe, K.; Wurstbauer, U.; Holleitner, A. W.; Kaniber, M.; Müller, K.; Finley, J. J. Direct exciton emission from atomically thin transition metal dichalcogenide heterostructures near the lifetime limit. *Sci. Rep.* **2017**, *7*, 12383.
- (13) Tartakovskii, A. Excitons in 2D heterostructures. *Nat. Rev. Phys.* **2020**, *2*, 8–9.
- (14) Tartakovskii, A. Moiré or not. *Nat. Mater.* **2020**, *19*, 581–582.
- (15) Bai, Y.; Zhou, L.; Wang, J.; Wu, W.; McGilly, L. J.; Halbertal, D.; Lo, C. F. L.; Liu, F.; Ardelean, J.; Rivera, P.; Finney, N. R.; Yang, X.-C.; Basov, D. N.; Yao, W.; Xu, X.; Hone, J.; Pasupathy, A. N.; Zhu, X.-Y. Excitons in strain-induced one-dimensional moiré potentials at transition metal dichalcogenide heterojunctions. *Nat. Mater.* **2020**, *19*, 1068–1073.
- (16) Dai, S.; Fei, Z.; Ma, Q.; Rodin, A. S.; Wagner, M.; McLeod, A. S.; Liu, M. K.; Gannett, W.; Regan, W.; Watanabe, K.; Taniguchi, T.; Thiemens, M.; Dominguez, G.; Neto, A. H. C.; Zettl, A.; Keilmann, F.; Jarillo-Herrero, P.; Fogler, M. M.; Basov, D. N. Tunable phonon polaritons in atomically thin van der Waals crystals of boron nitride. *Science* **2014**, *343*, 1125–1129.
- (17) Caldwell, J. D.; Kretinin, A. V.; Chen, Y.; Giannini, V.; Fogler, M. M.; Francescato, Y.; Ellis, C. T.; Tischler, J. G.; Woods, C. R.; Giles, A. J.; Hong, M.; Watanabe, K.; Taniguchi, T.; Maier, S. A.; Novoselov, K. S. Sub-diffractive volume-confined polaritons in the natural hyperbolic material hexagonal boron nitride. *Nat. Commun.* **2014**, *5*, 5221.
- (18) Tran, T. T.; Bray, K.; Ford, M. J.; Toth, M.; Aharonovich, I. Quantum emission from hexagonal boron nitride monolayers. *Nat. Nanotechnol.* **2016**, *11*, 37–41.
- (19) Tran, T. T.; Elbadawi, C.; Totonjian, D.; Lobo, C. J.; Gross, G.; Moon, H.; Englund, D. R.; Ford, M. J.; Aharonovich, I.; Toth, M. Robust multicolor single photon emission from point defects in hexagonal boron nitride. *ACS Nano* **2016**, *10*, 7331–7338.
- (20) Bourrillion, R.; Meuret, S.; Tararan, A.; Stéphan, O.; Kociak, M.; Tizei, L. H.; Zobelli, A. Bright UV single photon emission at point defects in h-BN. *Nano Lett.* **2016**, *16*, 4317–4321.
- (21) Vogl, T.; Lu, Y.; Koy Lam, P. Room temperature single photon source using fiber-integrated hexagonal boron nitride. *J. Phys. D: Appl. Phys.* **2017**, *50*, 295101.
- (22) Fournier, C.; Plaud, A.; Roux, S.; Pierret, A.; Rosticher, M.; Watanabe, K. W.; Taniguchi, T.; Buil, S.; Qulin, X.; Barjon, J.; Hermier, J.-P.; Delteil, H. Position-controlled quantum emitters with reproducible emission wavelength in hexagonal boron nitride. *Nat. Commun.* **2021**, *12*, 3779.
- (23) Wang, G.; Dai, Z.; Xiao, J.; Feng, S.; Weng, C.; Liu, L.; Xu, Z.; Huang, R.; Zhang, Z. Bending of multilayer van der Waals materials. *Phys. Rev. Lett.* **2019**, *123*, 116101.
- (24) Blundo, E.; Cappelluti, E.; Felici, M.; Pettinari, G.; Polimeni, A. Strain-tuning of the electronic, optical, and vibrational properties of two-dimensional crystals. *Appl. Phys. Rev.* **2021**, *8*, No. 021318.
- (25) Shandilya, P. K.; Fröch, J. E.; Mitchell, M.; Lake, D. P.; Kim, S.; Toth, M.; Behera, B.; Healey, C.; Aharonovich, I.; Barclay, P. E.

- Hexagonal boron nitride cavity optomechanics. *Nano Lett.* **2019**, *19*, 1343–1350.
- (26) Mendelson, N.; Doherty, M.; Toth, M.; Aharonovich, I.; Tran, T. T. Strain-Induced Modification of the Optical Characteristics of Quantum Emitters in Hexagonal Boron Nitride. *Adv. Mater.* **2020**, *32*, 1908316.
- (27) Duan, J.; Chen, R.; Li, J.; Jin, K.; Sun, Z.; Chen, J. Launching phonon polaritons by natural boron nitride wrinkles with modifiable dispersion by dielectric environments. *Adv. Mater.* **2017**, *29*, 1702494.
- (28) Androulidakis, C.; Koukaras, E.; Poss, M.; Papagelis, K.; Galiotis, C.; Tawfick, S. Strained hexagonal boron nitride: Phonon shift and Grüneisen parameter. *Phys. Rev. B* **2018**, *97*, 241414.
- (29) Cai, Q.; Scullion, D.; Falin, A.; Watanabe, K.; Taniguchi, T.; Chen, Y.; Santos, E. J.; Li, L. H. Raman signature and phonon dispersion of atomically thin boron nitride. *Nanoscale* **2017**, *9*, 3059–3067.
- (30) Khestanova, E.; Guinea, F.; Fumagalli, L.; Geim, A.; Grigorieva, I. Universal shape and pressure inside bubbles appearing in van der Waals heterostructures. *Nat. Commun.* **2016**, *7*, 12587.
- (31) He, L.; Wang, H.; Chen, L.; Wang, X.; Xie, H.; Jiang, C.; Li, C.; Elibol, K.; Meyer, J.; Watanabe, K.; Taniguchi, T.; Wu, Z.; Wang, W.; Ni, Z.; Miao, X.; Zhang, C.; Zhang, D.; Wang, H.; Xie, X. Isolating hydrogen in hexagonal boron nitride bubbles by a plasma treatment. *Nat. Commun.* **2019**, *10*, 2815.
- (32) Blundo, E.; Yildirim, T.; Pettinari, G.; Polimeni, A. Experimental Adhesion Energy in van der Waals Crystals and Heterostructures from Atomically Thin Bubbles. *Phys. Rev. Lett.* **2021**, *127*, No. 046101.
- (33) Di Giorgio, C.; Blundo, E.; Pettinari, G.; Felici, M.; Lu, Y.; Cuocolo, A. M.; Polimeni, A.; Bobba, F. Nanoscale Measurements of Elastic Properties and Hydrostatic Pressure in H<sub>2</sub>-Bulged MoS<sub>2</sub> Membranes. *Adv. Mater. Interfaces* **2020**, *7*, 2001024.
- (34) Di Giorgio, C.; Blundo, E.; Pettinari, G.; Felici, M.; Polimeni, A.; Bobba, F. Exceptional Elasticity of Microscale Constrained MoS<sub>2</sub> Domes. *ACS Appl. Mater. Interfaces* **2021**, *13*, 48228.
- (35) Zabel, J.; Nair, R. R.; Ott, A.; Georgiou, T.; Geim, A. K.; Novoselov, K. S.; Casiraghi, C. Raman spectroscopy of graphene and bilayer under biaxial strain: bubbles and balloons. *Nano Lett.* **2012**, *12*, 617–621.
- (36) Lloyd, D.; Liu, X.; Christopher, J. W.; Cantley, L.; Wadehra, A.; Kim, B. L.; Goldberg, B. B.; Swan, A. K.; Bunch, J. S. Band gap engineering with ultralarge biaxial strains in suspended monolayer MoS<sub>2</sub>. *Nano Lett.* **2016**, *16*, 5836–5841.
- (37) Tedeschi, D.; Blundo, E.; Felici, M.; Pettinari, G.; Liu, B.; Yildirim, T.; Petroni, E.; Zhang, C.; Zhu, Y.; Sennato, S.; Lu, Y.; Polimeni, A. Controlled Micro/Nanodome Formation in Proton-Irradiated Bulk Transition-Metal Dichalcogenides. *Adv. Mater.* **2019**, *31*, 1903795.
- (38) Blundo, E.; Di Giorgio, C.; Pettinari, G.; Yildirim, T.; Felici, M.; Lu, Y.; Bobba, F.; Polimeni, A. Engineered creation of periodic giant, non-uniform strains in MoS<sub>2</sub> monolayers. *Adv. Mater. Interfaces* **2020**, *7*, 2000621.
- (39) Blundo, E.; Felici, M.; Yildirim, T.; Pettinari, G.; Tedeschi, D.; Miriametro, A.; Liu, B.; Ma, W.; Lu, Y.; Polimeni, A. Evidence of the direct-to-indirect band gap transition in strained two-dimensional WS<sub>2</sub>, MoS<sub>2</sub>, and WSe<sub>2</sub>. *Phys. Rev. Res.* **2020**, *2*, No. 012024.
- (40) Tyurnina, A. V.; Bandurin, D. A.; Khestanova, E.; Kravets, V. G.; Koperski, M.; Guinea, F.; Grigorenko, A. N.; Geim, A. K.; Grigorieva, I. V. Strained bubbles in van der Waals heterostructures as local emitters of photoluminescence with adjustable wavelength. *ACS Photonics* **2019**, *6*, 516–524.
- (41) Androulidakis, C.; Galiotis, C. Thermomechanical behaviour of hexagonal boron nitride at elevated temperatures. *2D Mater.* **2020**, *7*, No. 045011.
- (42) Felton, J.; Blundo, E.; Ling, S.; Glover, J.; Kudrynskyi, Z. R.; Makarovskiy, O.; Kovalyuk, Z. D.; Besley, E.; Walker, G.; Polimeni, A.; Patanè, A. The Interaction of Hydrogen with the van der Waals Crystal  $\gamma$ -InSe. *Molecules* **2020**, *25*, 2526.
- (43) Lozada-Hidalgo, M.; Hu, S.; Marshall, O.; Mishchenko, A.; Grigorenko, A.; Dryfe, R.; Radha, B.; Grigorieva, I.; Geim, A. Sieving hydrogen isotopes through two-dimensional crystals. *Science* **2016**, *351*, 68–70.
- (44) Chejanovsky, N.; Rezai, M.; Paolucci, F.; Kim, Y.; Rendler, T.; Rouabeh, W.; Fávaro de Oliveira, F.; Herlinger, P.; Denisenko, A.; Yang, S.; Gerhardt, I.; Finkler, A.; Smet, J. H.; Wrachtrup, J. Structural Attributes and Photodynamics of Visible Spectrum Quantum Emitters in Hexagonal Boron Nitride. *Nano Lett.* **2016**, *16*, 7037–7045.
- (45) Choi, S.; Tran, T. T.; Elbadawi, C.; Lobo, C.; Wang, X.; Juodkazis, S.; Seniutinas, G.; Toth, M.; Aharonovich, I. Engineering and Localization of Quantum Emitters in Large Hexagonal Boron Nitride Layers. *ACS Appl. Mater. Interfaces* **2016**, *8*, 29642–29648.
- (46) Ziegler, J.; Klaiss, R.; Blaikie, A.; Miller, D.; Horowitz, V. R.; Alemán, B. J. Deterministic Quantum Emitter Formation in Hexagonal Boron Nitride via Controlled Edge Creation. *Nano Lett.* **2019**, *19*, 2121–2127.
- (47) Gu, R.; Wang, L.; Zhu, H.; Han, S.; Bai, Y.; Zhang, X.; Li, B.; Qin, C.; Liu, J.; Guo, G.; Shan, X.; Xiong, G.; Gao, J.; He, C.; Han, Z.; Liu, X.; Zhao, F. Engineering and Microscopic Mechanism of Quantum Emitters Induced by Heavy Ions in hBN. *ACS Photonics* **2021**, *8*, 2912–2922.
- (48) Fischer, M.; Caridad, J. M.; Sajid, A.; Ghaderzadeh, S.; Ghorbani-Asl, M.; Gammelgaard, L.; Bøggild, P.; Thygesen, K. S.; Krasheninnikov, A. V.; Xiao, S.; Wubs, M.; Stenger, N. Controlled generation of luminescent centers in hexagonal boron nitride by irradiation engineering. *Sci. Adv.* **2021**, *7*, No. eabe7138.
- (49) Mendelson, N.; Chugh, D.; Reimers, J. R.; Cheng, T. S.; Gottscholl, A.; Long, H.; Mellor, C. J.; Zettl, A.; Dyakonov, V.; Beton, P. H.; Novikov, S. V.; Jagadish, C.; Tan, H. H.; Ford, M. J.; Toth, M.; Bradac, C.; Aharonovich, I. Identifying carbon as the source of visible single-photon emission from hexagonal boron nitride. *Nat. Mater.* **2021**, *20*, 321–328.
- (50) Zhang, H.; Lan, M.; Tang, G.; Chen, F.; Shu, Z.; Chen, F.; Li, M. Discrete color centers in two-dimensional hexagonal boron nitride induced by fast neutron irradiation. *J. Mater. Chem. C* **2019**, *7*, 12211–12216.
- (51) Aslyamov, T.; Iakovlev, E.; Akhatov, I. S.; Zhilyaev, P. Model of graphene nanobubble: Combining classical density functional and elasticity theories. *J. Chem. Phys.* **2020**, *152*, No. 054705.
- (52) Jia, Z.; Dong, J.; Liu, L.; Nie, A.; Xiang, J.; Wang, B.; Wen, F.; Mu, C.; Zhao, Z.; Xu, B.; Gong, Y.; Tian, Y.; Liu, Z. Photoluminescence and Raman Spectra Oscillations Induced by Laser Interference in Annealing-Created Monolayer WS<sub>2</sub> Bubbles. *Adv. Opt. Mater.* **2019**, *7*, 1801373.
- (53) Wang, P.; Gao, W.; Cao, Z.; Liechti, K. M.; Huang, R. Numerical analysis of circular graphene bubble. *J. Appl. Mech.* **2013**, *80*, No. 040905.
- (54) Han, E.; Yu, J.; Annevelink, E.; Son, J.; Kang, D. A.; Watanabe, K.; Taniguchi, T.; Ertekin, E.; Huang, P. Y.; van der Zande, A. M. Ultrasoft slip-mediated bending in few-layer graphene. *Nat. Mater.* **2020**, *19*, 305.
- (55) Huth, F.; Govyadinov, A.; Amarie, S.; Nuansing, W.; Keilmann, F.; Hillenbrand, R. Nano-FTIR absorption spectroscopy of molecular fingerprints at 20 nm spatial resolution. *Nano Lett.* **2012**, *12*, 3973–3978.
- (56) Mastel, S.; Govyadinov, A. A.; de Oliveira, T. V.; Amenabar, I.; Hillenbrand, R. Nanoscale-resolved chemical identification of thin organic films using infrared near-field spectroscopy and standard Fourier transform infrared references. *Appl. Phys. Lett.* **2015**, *106*, No. 023113.
- (57) Shi, Z.; Bechtel, H. A.; Berweger, S.; Sun, Y.; Zeng, B.; Jin, C.; Chang, H.; Martin, M. C.; Raschke, M. B.; Wang, F. Amplitude- and phase-resolved nanospectral imaging of phonon polaritons in hexagonal boron nitride. *ACS Photonics* **2015**, *2*, 790–796.
- (58) Li, P.; Lewin, M.; Kretinin, A. V.; Caldwell, J. D.; Novoselov, K. S.; Taniguchi, T.; Watanabe, K.; Gaussmann, F.; Taubner, T. Hyperbolic phonon-polaritons in boron nitride for near-field optical imaging and focusing. *Nat. Commun.* **2015**, *6*, 7507.

- (59) Moore, S. L.; Ciccarino, C. J.; Halbertal, D.; McGilly, L. J.; Finney, N. R.; Yao, K.; Shao, Y.; Ni, G.; Sternbach, A.; Telford, E. J.; Kim, B. S.; Rossi, S. E.; Watanabe, K.; Taniguchi, T.; Pasupathy, A. N.; Dean, C. R.; Hone, J.; Schuck, P. J.; Narang, P.; Basov, D. N. Nanoscale lattice dynamics in hexagonal boron nitride moiré superlattices. *Nat. Commun.* **2021**, *12*, 5741.
- (60) Qian, J.; Luan, Y.; Kim, M.; Ho, K.-M.; Shi, Y.; Wang, C.-Z.; Li, Y.; Fei, Z. Nonequilibrium phonon tuning and mapping in few-layer graphene with infrared nanoscopy. *Phys. Rev. B* **2021**, *103*, L201407.
- (61) Schmidt, P.; Vialla, F.; Latini, S.; Massicotte, M.; Tielrooij, K.-J.; Mastel, S.; Navickaite, G.; Danovich, M.; Ruiz-Tijerina, D. A.; Yelgel, C.; Fal'ko, V.; Thygesen, K. S.; Hillenbrand, R.; Koppens, F. H. L. Nano-imaging of intersubband transitions in van der Waals quantum wells. *Nat. Nanotechnol.* **2018**, *13*, 1035.
- (62) Geick, R.; Perry, C. H.; Rupprecht, G. Normal Modes in Hexagonal Boron Nitride. *Phys. Rev.* **1966**, *146*, 543.
- (63) Gorbachev, R. V.; Riaz, I.; Nair, R. R.; Jalil, R.; Britnell, L.; Belle, B. D.; Hill, E. W.; Novoselov, K. S.; Watanabe, K.; Taniguchi, T.; Geim, A. K.; Blake, P. Hunting for Monolayer Boron Nitride: Optical and Raman Signatures. *Small* **2011**, *7*, 465–468.
- (64) Krecmarova, M.; Andres-Penares, D.; Fekete, L.; Ashcheulov, P.; Molina-Sánchez, A.; Canet-Albiach, R.; Gregora, I.; Mortet, V.; Martínez-Pastor, J. P.; Sánchez-Royo, J. F. Optical Contrast and Raman Spectroscopy Techniques Applied to Few-Layer 2D Hexagonal Boron Nitride. *Nanomaterials* **2019**, *9*, 1047.